Optical angular momentum transfer to microrotors fabricated by two-photon photopolymerization

Theodor Asavei, Vincent L.Y. Loke, Marco Barbieri, Timo A Nieminen, Norman R. Heckenberg, Halina Rubinsztein-Dunlop

Optical angular momentum transfer to microrotors fabricated by two-photon photopolymerization

2009 New J. Phys. 11 093021

(http://iopscience.iop.org/1367-2630/11/9/093021)

New Journal of Physics
The open-access journal for physics

Optical angular momentum transfer to microrotors fabricated by two-photon photopolymerization

Theodor Asavei[1], Vincent L Y Loke, Marco Barbieri[2], Timo A Nieminen, Norman R Heckenberg and Halina Rubinsztein-Dunlop

The University of Queensland, Quantum Science Laboratory, School of Mathematics and Physics, Queensland 4072, Australia
E-mail: asavei@physics.uq.edu.au, loke@physics.uq.edu.au and timo@physics.uq.edu.au

New Journal of Physics **11** (2009) 093021 (20pp)
Received 17 July 2009
Published 15 September 2009
Online at http://www.njp.org/
doi:10.1088/1367-2630/11/9/093021

Abstract. We design, fabricate and test optically driven microrotors a few microns in size. The rotors are trapped and rotated in optical tweezers using an LG_{02} Laguerre–Gaussian laser beam. We verify that we can accurately measure the total optical torque by measuring the spin angular momentum transfer for three different polarizations, by comparing the optical torque with the optical torque calculated using computational electrodynamics and the viscous drag torque determined from the rotation rate and computational fluid dynamics. The torque agrees with that expected from the design principles and electromagnetic modelling of the torque within the optical trap.

[1] Author to whom any correspondence should be addressed.
[2] Current address: Laboratoire Ch. Fabry, Institut d'Optique, Palaiseau, France.

Contents

1. Introduction

Microscopic particles with sizes ranging from 25 nm to 10 μm can be stably trapped in a tightly focussed laser beam due to gradient forces. This type of optical trap, also called optical tweezers, was first achieved by Ashkin *et al* (1986). Forces of the order of pN can be exerted on the trapped particles with mW of laser power. These forces arise from the exchange of linear momentum between the laser beam and the trapped particle. Since light can carry angular momentum, one could expect microscopic torques of the order of pN μm to be exerted as well on the trapped object due to optical angular momentum transfer.

Such torques have been demonstrated in optical tweezers (Friese *et al* 1998, He *et al* 1995a), and practical applications of optical torques have been developed (Bishop *et al* 2004, Cheng *et al* 2002, Deufel *et al* 2007, Moffitt *et al* 2008, Parkin *et al* 2007).

However, these have mostly made use of birefringent materials, which restrict the range of materials that can be used, leading to difficulty in finding one with an appropriate combination of chemical, physical and optical properties, or shape-birefringent objects, resulting in low torque efficiencies, typically from $Q_\tau = 0.01$ to 0.05 (Bishop *et al* 2004). (The torque efficiency Q_τ is a dimensionless quantity giving the torque τ as the normalized change in angular momentum flux of the beam. For a beam of power P and angular frequency ω, the torque is $\tau = Q_\tau P/\omega$; this is equivalent to an angular momentum transfer of $Q_\tau\hbar$ per photon (Bishop *et al* 2003, Nieminen *et al* 2001).)

A solution to these difficulties that has emerged is to use synthetic micro-objects, which have usually been fabricated using two-photon photopolymerization (Maruo and Fourkas 2008, Park *et al* 2009). This allows the production of complex structures that can generate torque using the orbital angular momentum (OAM) of light, making it possible to exceed, in principle, the maximum angular momentum transfer of $2\hbar$ per photon if spin angular momentum (SAM) alone is employed.

Fabrication offers further advantages; the possibility of rotating particles in optical tweezers offers new perspectives for studying properties of biological molecules such as elasticity and torsional stiffness of DNA or torque generated by molecular motors (Moffitt *et al* 2008). In order to perform these studies, the molecule has to be attached with

one end to a fixed surface and with the other to an object that can be easily optically trapped and rotated in the optical trap. Even if we restrict ourselves to two-photon photopolymerization, there is a wide range of biocompatible materials suitable for the attachment of biomolecules available, and their size can be easily tailored to the studied systems.

The production, trapping and rotation of such structures has been demonstrated by a number of groups around the world (Gauthier 2001, Galajda and Ormos 2001, 2002, Higurashi *et al* 1994, Knöner *et al* 2007, Ukita and Kanehira 2002, Ukita and Nagatomi 2003). However, what is required is the development of initial designs and their evaluation, prior to further engineering and optimization. While it is possible to use computational electromagnetics to calculate the optical forces and torques acting on structures, this can require, with current computational capabilities, a major investment in time and effort or computational resources. Such computational techniques can make their most effective and efficient contribution through optimization and improvement of an existing design, rather than through the creation of the initial design *ex nihilo*. Here, we report the successful test of the practical application of, firstly, a simple method for the initial design of optically driven microrotors—treating the rotors as microholograms altering the angular momentum content of the driving beam—and, secondly, the evaluation of a fabricated microrotor using optical measurement of the total optical torque and computational modelling of the fluid flow to determine the viscous drag. The rotor performed as expected, and in agreement with computational electromagnetic modelling of the optical torque. Finally, we comment further on the design of optical microrotors.

2. The design of optical microrotors

The shape of a particle plays a central role in its interaction with light. Perhaps the most important aspect is the symmetry of the particle—consideration of the effects of particle symmetry allows some quite general aspects of optical torque to be understood (Nieminen *et al* 2009, Nieminen *et al* 2004). Essentially, if a scatterer possesses pth-order discrete rotational symmetry, incident light with $m_0\hbar$ angular momentum per photon about the symmetry axis of the particle, including both SAM and OAM, will be scattered into modes with $m_i\hbar$ angular momentum per photon, where $m_i = m_0 - ip$, where i is an integer. This is the rotational analog of the scattering of a plane wave by a periodic structure into a discrete plane wave spectrum, with a similar relationship for the transverse linear momentum of the modes.

In the case most typical of optical tweezers, the beam incident on the objective carries a well-defined OAM per photon (zero for a Gaussian beam, $\ell\hbar$ per photon for a Laguerre–Gauss mode of order ℓ (Allen *et al* 1992)). We can consider the beam to be composed of two circularly polarized components, such that the total angular momentum per photon is $\ell \pm 1$ for each of the two components. Recognizing that a rotationally symmetric optical system will not alter the angular momentum per photon (Nieminen *et al* 2008, Waterman 1971), this must also be the total angular momentum content of the non-paraxial trapping beam at the focus. A convenient way to represent such a non-paraxial beam is as a superposition of vector spherical wavefunctions (VSWFs) (Nieminen *et al* 2003), which have an azimuthal phase variation of $\exp(\mathrm{i}m\phi)$, where m is the azimuthal mode index, with the z-component of the angular momentum being equal to $m\hbar$ per photon. Thus, the non-paraxial VSWF representation of the beam will consist of modes with $m = \ell \pm 1$.

Thus, for pth-order rotational symmetry, incident modes will scatter into modes with $m = \ell \pm 1, \ell \pm 1 \pm p, \ell \pm 1 \pm 2p, \ell \pm 1 \pm 3p$, etc. For particles with $p = 2$, such as elongated

or flattened particles, the left- and right-circular incident modes will scatter into the same set of modes, resulting in interference, and therefore affecting the polarization of the scattered light—this gives rise to the shape birefringence of such particles. On the other hand, if $p > 2$, the scattered modes corresponding to the incident circular polarizations are distinct, and this interference will not occur, and the incident polarization will only be affected weakly. In this case, torque will be primarily due to OAM. Due to the absence of interference, the total torque due to the combination of left- and right-circular modes (e.g. if the incident beam is plane or elliptically polarized) will be the sum of the torques due to each circular polarization.

An important consequence of this is that Parkin's method (Parkin *et al* 2006) for measuring the total optical torque from measurements of the rotation rate and spin torque for left- and right-circular and plane polarizations can be expected to be accurate if the spin torque due to plane polarization is very small (which indicates very similar scattering of the left- and right-circular modes).

We can assume that the coupling of incident modes with small $|m|$ will usually be stronger than for high $|m|$ modes. Thus, an object illuminated by light carrying OAM will usually experience a torque (except in special cases, including when opposing spin reduces the total angular momentum to zero). If the object is mirror symmetric (i.e. achiral), then the scattering is independent of the handedness of the angular momentum, that is, the coupling of, e.g. m_1 to m_2 is the same as from $-m_1$ to $-m_2$. Therefore, an achiral rotor with $p > 2$ will experience no torque in a plane polarized Gaussian beam. Such a rotor will be ideal for illumination by Laguerre–Gauss beams, and will be equally rotatable in both the directions. A chiral rotor, on the other hand, can rotate in a Gaussian beam, but will generally rotate at different speeds when illuminated by Laguerre–Gauss beams of opposite handedness.

In optical tweezers, since trapped objects are only weakly reflecting, the majority of the scattered light is the forward-transmitted light. The coupling to the different scattered modes will depend strongly on the phase variations in the transmitted light. Therefore, we can productively view optically driven rotors as microscopic holograms—the thickness of the structure should ensure a large phase difference between light that passes through the structure, and light that does not.

If, for example, we consider an on-axis hologram of the type that can be used for the conversion of Gaussian beams into Laguerre–Gauss beams (Heckenberg *et al* 1992b); as shown in figure 1, we see that exactly the symmetry considerations apply. In the example shown in figure 1, a Gaussian beam will be converted into an LG_{04} beam, or an $LG_{0,-4}$ beam, depending on whether the incident beam is converging or diverging; note that the hologram is a normalized interference pattern between an LG_{04} mode and a spherical wave). In general, both LG_{04} and $LG_{0,-4}$ modes will be present, along with a zero-order LG_{00} (i.e. a Gaussian component), higher azimuthal order modes such as $LG_{0,\pm 8}$ modes, and higher order radial modes.

In the case of a macroscopic hologram interacting with a paraxial beam, we do not need to consider any change in polarization at all. This is the only important difference between this macroscopic case and the microscopic non-paraxial case of an optically driven microrotor. In the latter case, rather than considering the orbital angular momentum of each component, we need to consider the total angular momentum of each component, given by the azimuthal mode index m.

Therefore, we can productively view optically driven rotors as microscopic holographic mode converters. A simple possible design of a microrotor, shown in figure 2(b), is based on the hologram shown in figure 1. The key difference is the solid central region, for structural

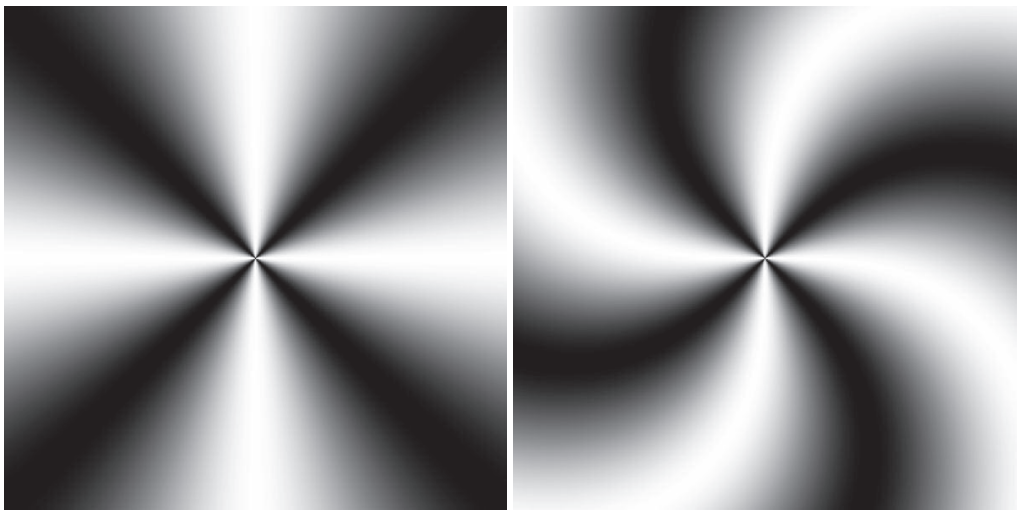

(a) (b)

Figure 1. On-axis holograms for the generation of $LG_{0,\pm4}$ Laguerre–Gauss beams. (a) An achiral hologram such as shown here will, when illuminated by a Gaussian beam, produce equal amplitude $LG_{0,-4}$ and $LG_{0,+4}$ components in the transmitted beam, with no reaction torque. A blazed hologram could be used to increase the amplitude of one of these modes, and decrease the other. (b) A chiral hologram such as this is the interference pattern between an $LG_{0,+4}$ beam and a diverging spherical wave, or an $LG_{0,-4}$ beam and a converging spherical wave. Therefore, the curvature of the wavefronts of an illuminating Gaussian beam can be controlled to produce torque in either direction.

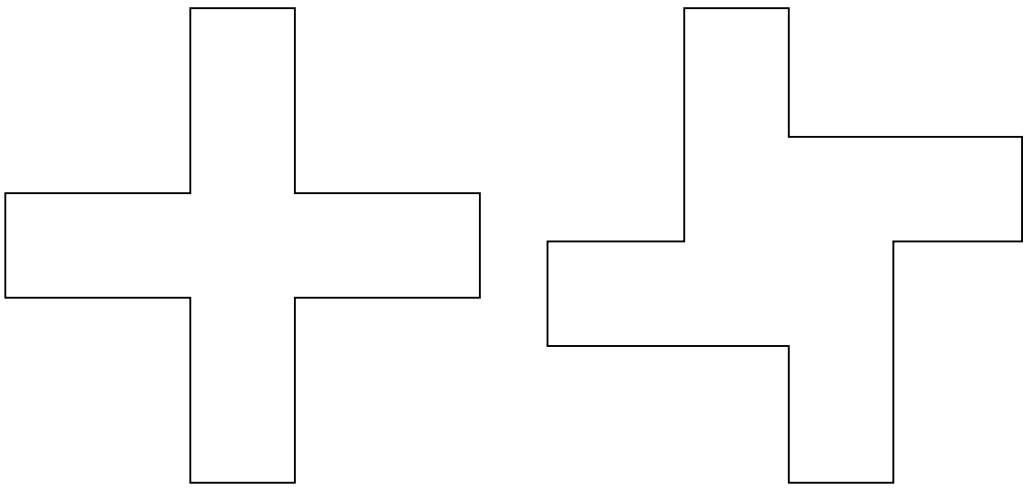

(a) (b)

Figure 2. Simple planar structures that are binary approximations of the holograms in figure 1. (a) Achiral. (b) Chiral.

integrity. For a chiral structure like this, the symmetry of scattering to positive and negative orders of scattering (i.e. to $m < m_0$ and $m > m_0$) will differ, and a torque will result from the generation of orbital angular momentum by scattering by the structure. Therefore, a structure of this type can be rotated by a Gaussian beam.

However, if we wish to have a structure that can be rotated with equal torque in either direction, we need to avoid a chiral shape, and have particles that are mirror symmetric about a plane containing the axis of rotational symmetry, in which case the coupling from $m_0 = 0$ to $\pm m$ will be identical, since these modes are mirror images of each other. A structure of this type is shown in figure 2(a). This type of structure is ideal for driving with a beam-carrying OAM. If, in this case, the incident beam has $m_0 = +2$, there will be significant scattering to VSWF modes with $m = -2$, and a torque will result. The direction of the applied torque can be reversed by changing the handedness of the driving beam.

As discussed earlier, a structure with discrete rotational symmetry with $p > 2$, illuminated by a beam with $m = \ell \pm 1$, experiences a torque that is independent of the rotational position of the particle. This same result can also be deduced directly from the symmetry, since the effective polarizability in the x–y plane of such a particle can be written as $\alpha\mathbf{I}$ where α is a constant scalar, and $\mathbf{I}$ is a 2×2 identity tensor.

On the other hand, for an elongated or flattened particle, with $p = 2$, there will be interference between the left- and right-hand scattered modes, and the torque due to a linearly polarized beam will be angle dependent. This effect can be thought of as the mechanism responsible for the shape birefringence of such particles.

More generally, a beam with zero angular momentum can be a superposition of modes with opposing orbital angular momentum, as well as modes with opposing circular polarization (Parkin *et al* 2004). In this case, the difference in orbital angular momentum between left- and right-handed modes can be other than $2\hbar$ per photon. Thus, interference between the left- and right-hand scattered modes can result in angle-dependent torques acting to align the structure, even for $p > 2$—higher-order rotational symmetry does not rule out the use of orbital angular momentum for alignment. Notably, alignment of this type has seen extensive use for the generation of optical torque (Bingelyte *et al* 2003, Paterson *et al* 2001, Sato *et al* 1991).

However, if alignment is the desired outcome, it is best if the structure is not chiral, since a chiral structure will generate an angle-independent torque that will compete with the angle-dependent alignment torque. Thus, the choice between a chiral and an achiral structure is largely a choice between efficiency and flexibility. A chiral structure will typically result in a higher torque efficiency, generating more torque for the same power, while an achiral structure allows greater controllability, allowing equal torques for both left- and right-handed rotation, and can be operated both by angle-dependent alignment and angle-independent spinning. In addition, with $p > 2$, the structure can be trapped with no torque, angle-dependent or otherwise, in, for example, a linearly polarized Gaussian beam.

Since the achiral rotor with $p > 2$ offers an interesting and complex range of behaviour, we will use such a structure to demonstrate the action of orbital angular momentum, and also demonstrate zero torque when trapping using a plane polarized Gaussian beam. From the above principles, we can do this with a four-armed, mirror-symmetric rotor. A practical issue is that the symmetry axis of the rotor should coincide with the beam axis. This can be ensured by using a central stalk which will align along the beam axis. For a typical photopolymerized object in water, we have refractive indices of approximately $n_{\mathrm{obj}} = 1.50$–1.55 for the object and $n_{\mathrm{med}} = 1.33$ for the surrounding water. To obtain a phase difference of close to a half-wave, we

want a thickness of $\lambda_{med}/(2(n_{obj} - n_{med}))$, where λ_{med} is the wavelength in the medium. This is a thickness of approximately double the free-space wavelength of the trapping beam.

3. Fabrication

The two-photon photopolymerization technique was pioneered by Strickler and Webb in 1991, following the application of two-photon excitation in laser scanning fluorescence microscopy (Denk *et al* 1990). Two-photon excitation was used to record high-density digital information in a multilayered three dimensional (3D) format by writing of submicrometre size voxels in a photopolymer with femtosecond infrared (IR) laser pulses (Strickler and Webb 1991). The first 3D-microfabricated structures with two-photon photopolymerization were reported in 1997 (Maruo *et al* 1997). Since then, various micromachines have been produced (micropumps, microgears and microneedles) with resolution of the order of 100 nm (Galajda and Ormos 2001, Maruo and Inoue 2006, Maruo *et al* 2003). The method has been recently reviewed (Maruo and Fourkas 2008, Park *et al* 2009). Our own photopolymerization setup and its performance has been described by Asavei *et al* (2009).

We produce the microrotors using two-photon photopolymerization of NOA63 resin from Norland Products. The 3D object is represented by 2D layers (bitmaps) corresponding to the areas that need to be polymerized. The program controlling the scanning stage reads the bitmap files and the resin is exposed (the shutter is opened) when the pixel in the bitmap is black (has value 0) and the shutter closes when the pixel is white (has value 1). Three-dimensional structures are obtained by moving the sample in the z-direction after each x–y scan. The bitmap resolution is set to 100×100 pixels which corresponds to $10 \times 10\,\mu$m travel in the x- and y-directions hence each individual pixel is $100 \times 100\,\text{nm}^2$ in size giving a lateral resolution of 100 nm. The axial resolution is 200 nm given by the offset in the z-direction. The 3D computer design and the 2D layers of our microrotors are shown in figure 3, along with a scanning electron micrograph of an actual rotor.

The size of the squares defining the stalk is chosen to be 18×18 pixels and the cross is 54×54 pixels. The whole object is composed of 41 layers.

After the polymerization, the unexposed resin is washed off with acetone, leaving the 3D structure attached to the cover slip. An scanning electron microscope (SEM) image of a typical rotor is shown in figure 4.

4. Optical trapping and rotation

After production, the structures were used for rotation in optical tweezers. The goal of these experiments is to measure the torque exerted on the microstructures by the trapping beam through transfer of optical angular momentum.

Optical trapping is performed in an inverted microscope built in-house. The trapping laser is a 5 W, 1070 nm Nd:YAG fibre laser (IPG Photonics, Oxford, MA, USA). It is focused on the sample by a 100× Olympus oil immersion objective lens with high numerical aperture (N.A. = 1.3). The output power is controlled by a half-wave plate ($\lambda/2$) and a polarizing beam splitter (PBS) cube. The sample is imaged onto a charge coupled device (CCD) camera by the same objective lens.

The angular momentum of the incident trapping beam is controlled by using a quarter wave plate ($\lambda/4$) for SAM and a computer generated hologram (He *et al* 1995) creating

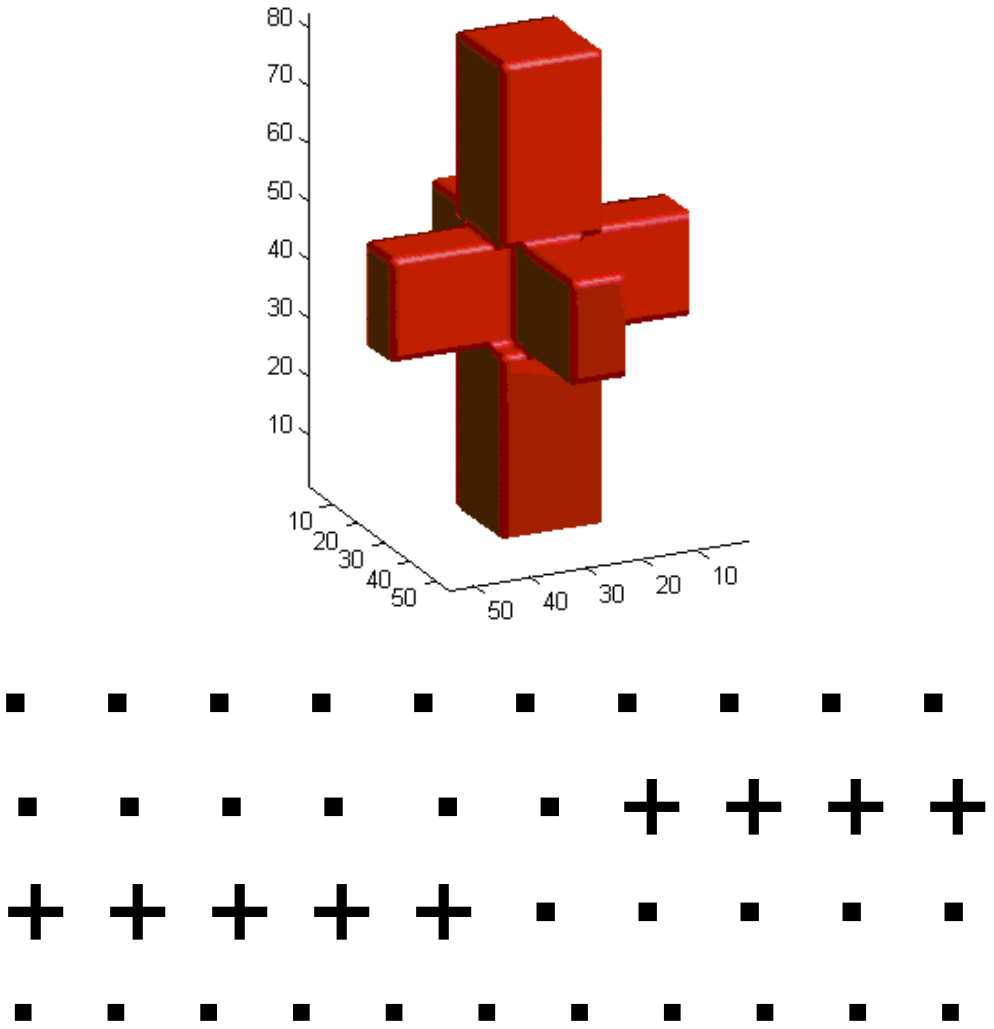

Figure 3. (top) 3D computer-aided design (CAD) model of the microfabricated object, and (bottom) the sequence of 2D bitmaps defining the 3D object.

Laguerre–Gauss modes (designated as $LG_{p\ell}$, where p is the radial mode index, and ℓ is the azimuthal mode index) for OAM. In our experiments we used a hologram which generates LG_{02} modes in the first order when the incident beam is the TEM_{00} Gaussian beam of the laser. These modes have an OAM of $2\hbar$ per photon. The hologram we used here was produced photographically (Parkin *et al* 2004), but a spatial light modulator (SLM) or other means of generating beams with OAM could be used instead.

The hologram was mounted on an xyz translation stage for fine adjustments. The output mode is imaged onto a CCD camera while adjusting the hologram. Figure 5 shows CCD camera photographs of an LG_{02} mode and incident Gaussian beam respectively.

Demineralized water is then added to immerse the rotor, which is then placed on the sample stage of the trap. The trapping system uses a water-immersion condenser, which allows the top of the sample to remain open (recall that the trap is based on an inverted microscope); this allows mechanical access to the sample. The microstructure can then be easily detached by touching it

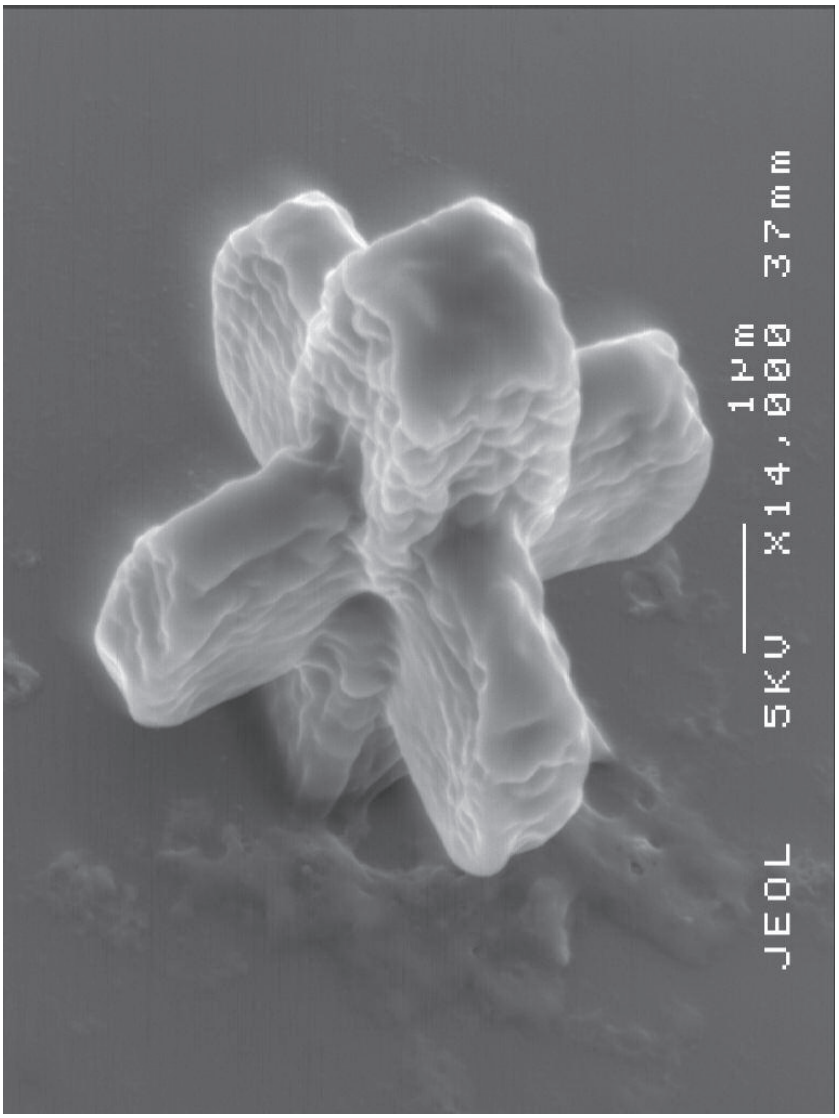

Figure 4. An SEM image of the microfabricated structure attached to the cover slip.

with the tip of a needle mounted on a translation stage. The freed structure then floats close to the cover slip surface. Thus we can observe the shape of the formed structure and the resemblance with the CAD model by means of bright field microscopy as shown in figure 6.

The structure is easily trapped and starts to rotate in the focus of the beam-carrying angular momentum. The rotation rate is in the order of 1 Hz for a trapping beam power of 20 mW at the sample. The structure does not rotate when trapped in a Gaussian beam.

5. Optical measurement of torque

The torque exerted on the microstructure is the sum of the two contributions from SAM and OAM transfer.

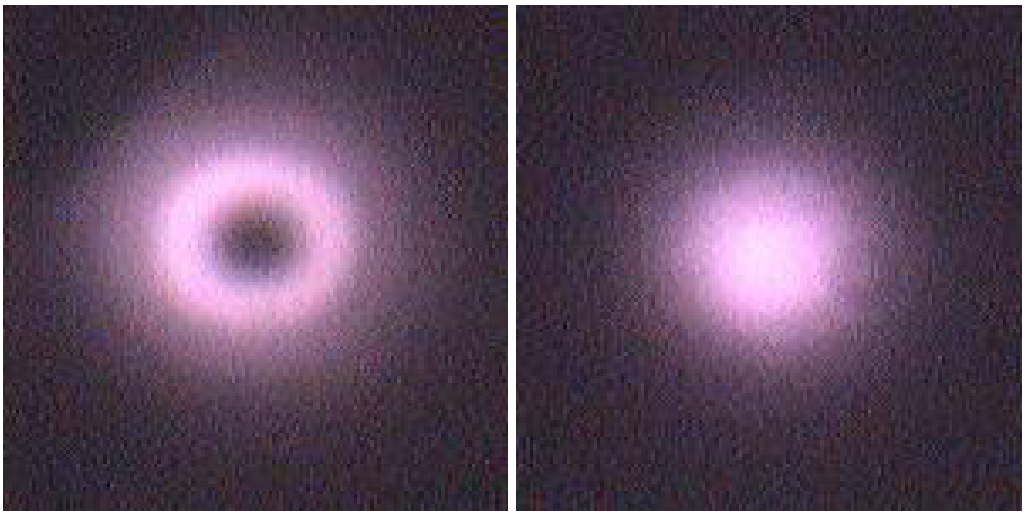

Figure 5. CCD camera photograph of the LG_{02} mode (a) and the TEM_{00} Gaussian beam (b).

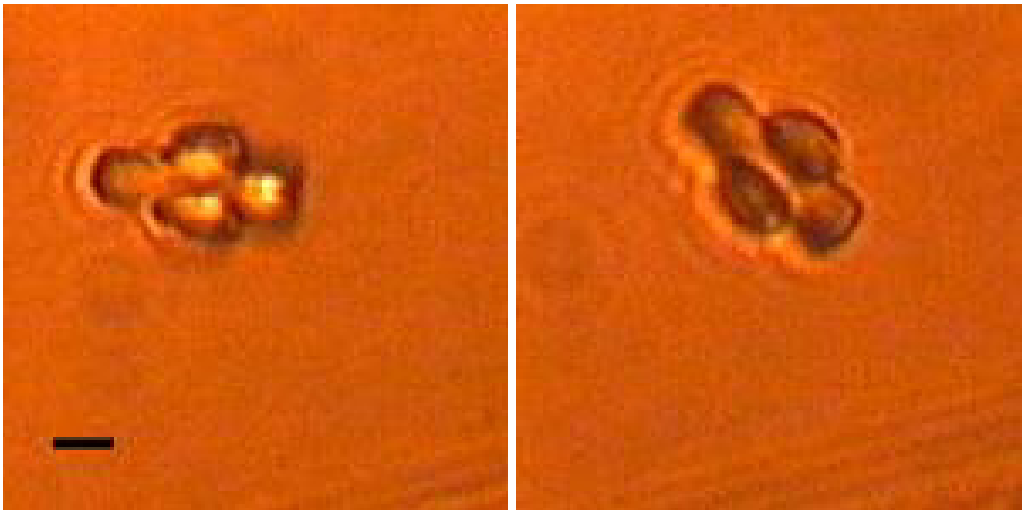

Figure 6. Bright-field microscope images of the microstructure floating freely in solution after being detached from the cover slip. Scale bar is 2 μm.

The spin torque measurement is based on the fact that any coherent beam can be represented as a sum of two circularly polarized components with opposite handedness with a coefficient of circular polarization σ_s given by $\sigma_s = (P_L - P_R)/P$, where P_L and P_R are the powers of the left and right circularly polarized components respectively and P is the total power of the beam (Nieminen *et al* 2001). Therefore the spin torque τ_s can be written as $\tau_s = \Delta\sigma_s P/\omega$, with $\Delta\sigma_s$ being the change in the coefficient of circular polarization due to the SAM transfer, P is the incident beam power and ω is the optical angular frequency of the beam. Hence by measuring $\Delta\sigma_s$ and knowing P and ω, the torque can be found. The change in the coefficient of circular polarization is measured by two photodetectors (PD1 and PD2) which are placed after a PBS cube. The outgoing beam is focussed by the condenser and then split into two orthogonal

linearly polarized components by the quarter wave plate ($\lambda/4$) and the cube. The two linearly polarized components correspond to the left and right circularly polarized components of the outgoing beam. The two detectors measure the power of each beam and hence the coefficient $\Delta\sigma_s$ can be found which is directly related to the spin torque per photon. From the above mentioned equation $\tau_s = \Delta\sigma_s P/\omega$, writing $P = N\hbar\omega$ with N being the number of photons per time, one can find out that the spin torque per photon has the value of $\Delta\sigma_s\hbar$.

Similarly to the spin component of the torque, one can write the orbital torque τ_o as being $\tau_o = \Delta\sigma_o P/\omega$, with $\Delta\sigma_o$ being a coefficient related to the orbital torque per photon in the same way as $\Delta\sigma_s$ is related to the spin torque per photon. Thus the orbital torque per photon has the value of $\Delta\sigma_o\hbar$.

In order to measure the orbital torque τ_o, we used a method previously described in the literature (Parkin *et al* 2006). It is based on the steady rotation of the microstructure, which means that the total optical torque is equal to the drag torque due to rotation in the liquid. In our case the surrounding medium behaves as a Newtonian fluid and hence the drag torque is proportional to the rotation rate Ω. Note that the structure is trapped well clear of any surfaces so that no corrections for frictional forces or wall effects need to be made.

We can write the following equation for the total torque τ:

$$\tau = \tau_s + \tau_o = D\Omega, \tag{1}$$

where D is the rotational drag coefficient for the microstructure in the fluid. From equation (1) one can calculate τ_o and D by measuring τ_s and Ω for three different degrees of polarization of the incident light (left-handed, right-handed and linearly polarized light). Just as the torque efficiency provides a power-independent description of the optical torque, it can be useful to introduce a spin torque efficiency Q_s, such that $\tau_s = Q_s P/\omega$, and an orbital torque efficiency Q_o such that $\tau_o = Q_o P/\omega$.

The intensity variation at an off-axis point in the transmitted beam is also measured. Due to the symmetry of the structure, the rotation rate is one quarter of the signal frequency. This is a much easier method for measuring the rotation rate than frame by frame video microscopy. An example of a measured signal for a structure rotating at about 2 Hz is shown in figure 7. With a laser power of $P = 40$ mW at the focus, our rotation frequency varied from 2.25 Hz (right-circular) to 3 Hz (left-circular), with an uncertainty of 5%.

Parkin's method (Parkin *et al* 2006) was used to measure the total optical torque, including the contribution due to OAM. The relationship between rotation rate and the spin component of the torque is shown in figure 8. Since the spatial structure of the beam is the same for all three polarizations (left circular, right circular and linear), we can assume that the orbital torque is the same for all three, and the only difference in torque is due to the different spin torques, which are measured optically. The difference in rotation rates due to the different spin torques allows us to find the rotational drag coefficient, and hence the total torque from the rotation rates. We find that the orbital torque efficiency is 0.20 ± 0.03, and the orbital torque is 4.8 ± 0.7 pN μm, which is 10 times higher than the spin component. For a plane-polarized incident beam, this is also the total torque.

6. Performance of the microrotor

Qualitatively, the rotor performs as expected. The structure rotates when trapped in a beam-carrying OAM, does not rotate in a Gaussian beam, and the torque efficiency of 0.2 is

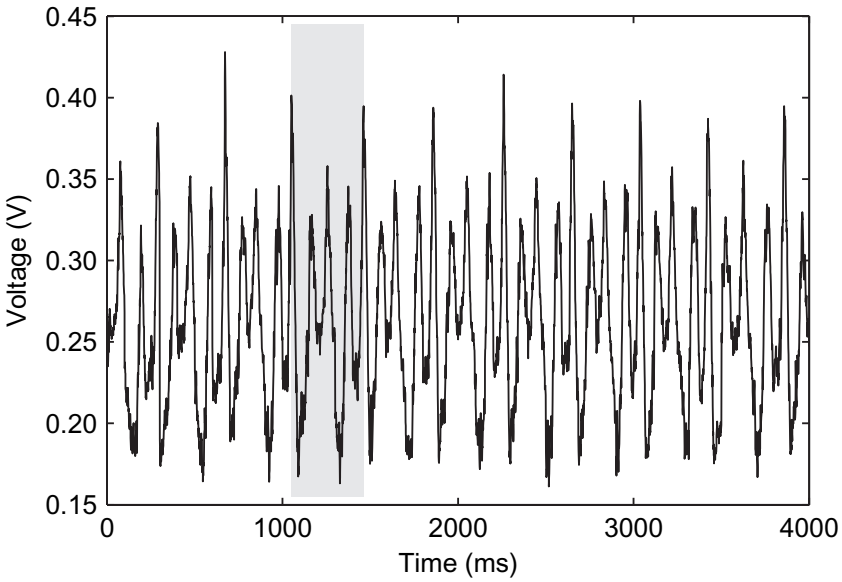

Figure 7. A typical photodiode signature measuring the rotation frequency of the trapped microstructure. The rotation period is marked by the two arrows and shows the fourfold symmetry characteristic of the rotor.

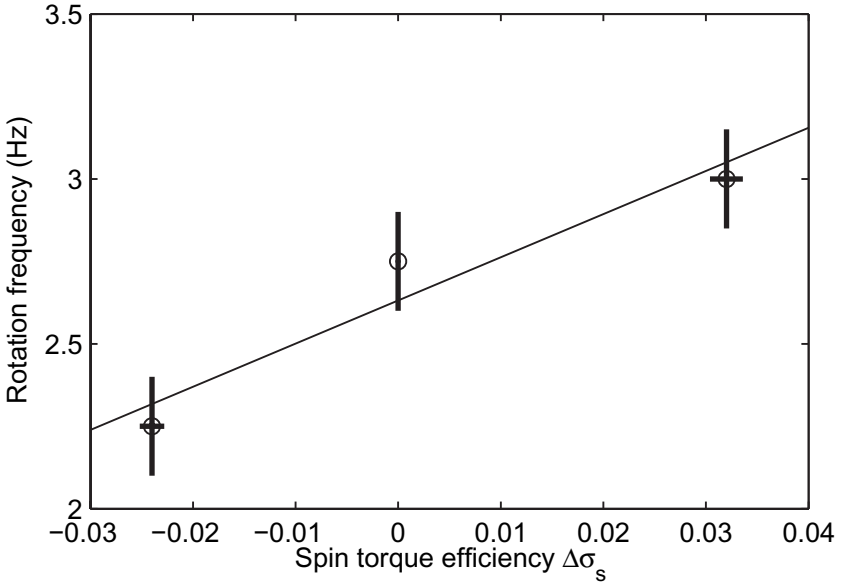

Figure 8. The rotation frequency of the trapped rotor as a function of the spin torque per photon for three different polarizations (left circular, right circular and linear). From the fit to the data, the orbital torque per photon is found.

much higher than that typical for shape-birefringent objects (e.g. 0.02–0.05). We can apply two quantitative tests: comparison between the measured optical torque and the computationally predicted optical torque, and comparison between the measured optical torque and the viscous drag torque found from the measured rotation rate and the computationally determined viscous drag coefficient.

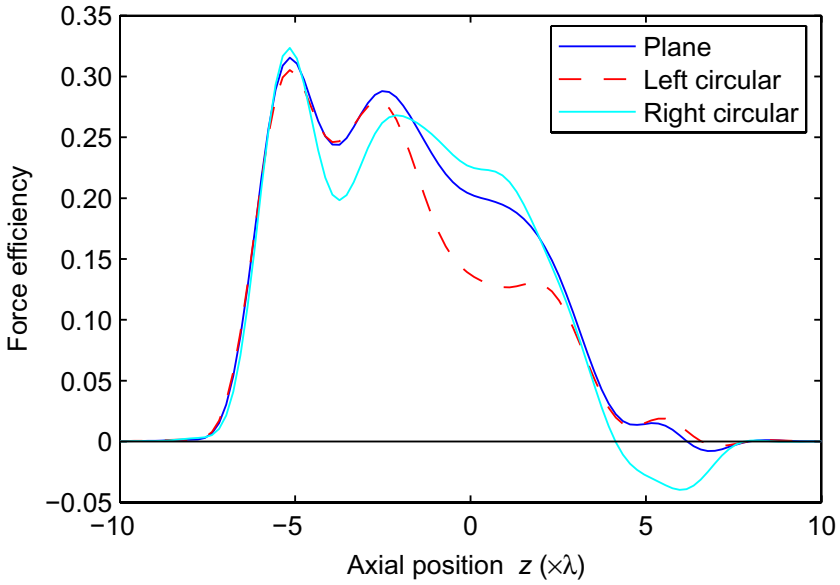

Figure 9. Axial optical force acting on rotor as a function of position along the beam axis. The predicted equilibrium points are where the curves cross the zero force efficiency line (horizontal straight line) from above.

6.1. Prediction of optical torque using computational electromagnetics

The optical force and torque acting on a known arbitrary structure can, in principle, be calculated using electromagnetic theory. In practice, this must be done computationally, which places limits especially on the size of the structures. However, optical microrotors are usually only of the order of several wavelengths in size, and the computation is feasible.

We use a variation of the discrete dipole approximation (DDA), modified to generate the T-matrix (Mishchenko *et al* 2000, Waterman 1971) and making use of optimizations based on the discrete rotational symmetry (Loke *et al* 2009). The resulting T-matrix can be used in our optical tweezers toolbox (Nieminen *et al* 2007) to calculate the optical forces and torques.

An important element in the calculation which is difficult to measure precisely is the structure of the incident illumination (figure 5(a)). While this beam carries $2\hbar$ OAM per photon, the radial variation of the intensity is not exactly that of a pure LG_{02} mode (Heckenberg *et al* 1992a). From our measurement of the intensity profile of the beam, and the width of the back aperture of the objective, which is slightly underfilled, we estimate that the beam is approximately equivalent to a pure LG_{02} mode focussed by an optimally filled objective of numerical aperture 1.26 (expressing the equivalent beam in this form simplifies calculation of the beam in our optical tweezers toolbox (Nieminen *et al* 2003, 2007)). The resulting forces and torques are shown in figures 9 and 10. The equilibrium trapping position are where the axial force goes to zero, and is different for each polarization. However, the torque efficiency predicted at the equilbrium positions is 0.2, for all three polarizations—while the torque versus axial position is different for each polarization, the different axial equilibrium positions result in very similar torques for the three polarizations, in this particular case. This agrees closely with the optically measured torque.

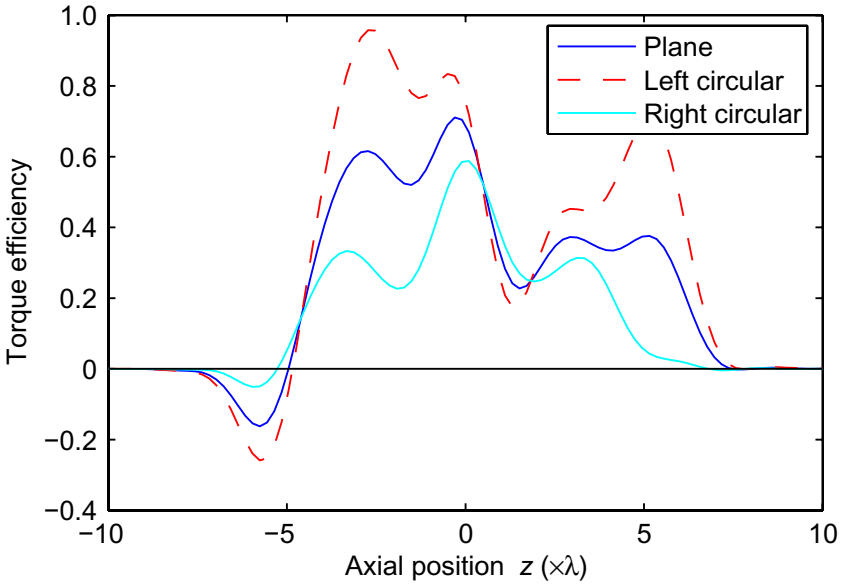

Figure 10. Optical torque acting on rotor as a function of position along the beam axis. The torque efficiency at the equilibrium positions is 0.2 (for all three polarizations).

6.2. Modelling of the fluid flow

Since the microrotor is small, and immersed in a viscous fluid, the resulting Reynolds numbers are small (for example, 10^{-8} for a rotor of diameter 10 μm rotating in water at 100 Hz), and we can assume the flow is well described by the Stokes approximation (i.e. creeping flow). In the interests of computational efficiency, it is highly desirable to reduce the problem to one of steady-state flow. For a rotating rotor, this can be accomplished by performing the calculation in a rotating reference frame in which the rotor is at rest. Since, in the Stokes limit, we can neglect inertial forces, we can also neglect the 'fictitious' forces (such as Coriolis forces) in the rotating frame. In this case, the Navier–Stokes equations reduce to the Laplace equation, $\nabla^2\vec{v} = 0$, where $\vec{v}$ is the flow velocity.

However, even in this simple form, the equation has an analytical solution for only a limited number of objects (sphere, spheroid and infinite cylinder). Thus in order to compare the experimental results of the optical torque with the counteracting drag torque we need to perform hydrodynamic simulations of the fluid flow generated by the rotating object of arbitrary shape.

We used the program FlexPDE (PDE Solutions Inc, Antioch, CA) which is a partial differential equation solver based on finite element numerical analysis. The program constructs a tetrahedral finite element mesh over the geometry specified by the user and then solves the differential equation numerically refining the mesh and the solution until the user-defined error bound is achieved (*FlexPDE 5.0 User Guide* 2005). A typical mesh is shown in figure 11.

Thus, the flow field can be simulated and the drag torque τ_d, which is the shear torque exerted by the fluid, can be found by integrating the shear stress tensor multiplied by the distance from the centre of rotation, over the rotating surface of the microstructure:

$$\tau_d = \int \sigma_{ik} x_i \mathrm{d}A_k, \tag{2}$$

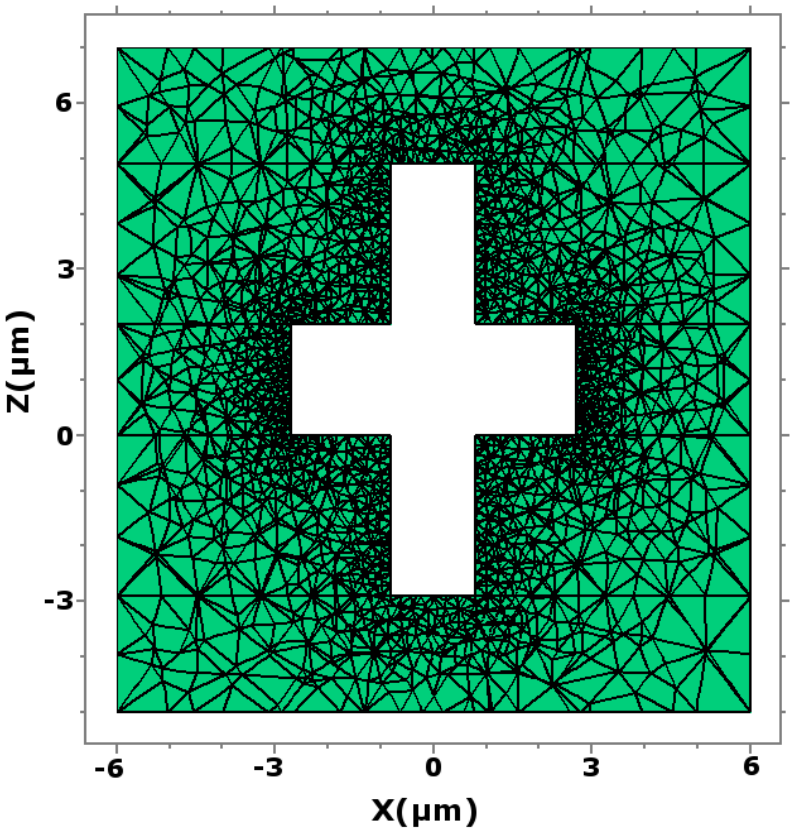

Figure 11. Cross section of the simulated surrounding medium through the x–z plane, which was chosen to be a cylinder with a diameter and height of 12 μm.

where x_i is the distance in the i-direction, $\mathrm{d}A_k$ is the surface element in the k-direction and σ_{ik} is the shear stress tensor

$$\sigma_{ik} = \eta \left(\frac{\partial v_i}{\partial x_k} + \frac{\partial v_k}{\partial x_i} \right). \tag{3}$$

Since the flow is steady state, there is a constant angular momentum flux through every closed surface surrounding the rotor, and the drag torque can be found by integrating the drag torque per unit area over *any* closed surface surrounding the rotor. Therefore, we can choose a simple surface, the shape of which can be independent of the rotor, over which to calculate the torque, greatly simplifying the calculation of the torque from the flow field.

The geometry chosen for our system was such that the microstructure was enclosed within a cylinder with a diameter and height of 12 μ. The shear stress at this outer cylindrical surface was used to calculate the drag torque.

The method was validated by comparing computational and analytical results for the drag on a rotating sphere. The difference between the simulation and the analytical solution was less than 0.5%, demonstrating that the finite size of the surrounding cylindrical surface introduces only a small error.

Typical results for the flow are shown in figure 12, where we show the flow field around the rotating object is simulated as well as the shear stress field (the shear force acting per unit area), which is used to calculate the torque.

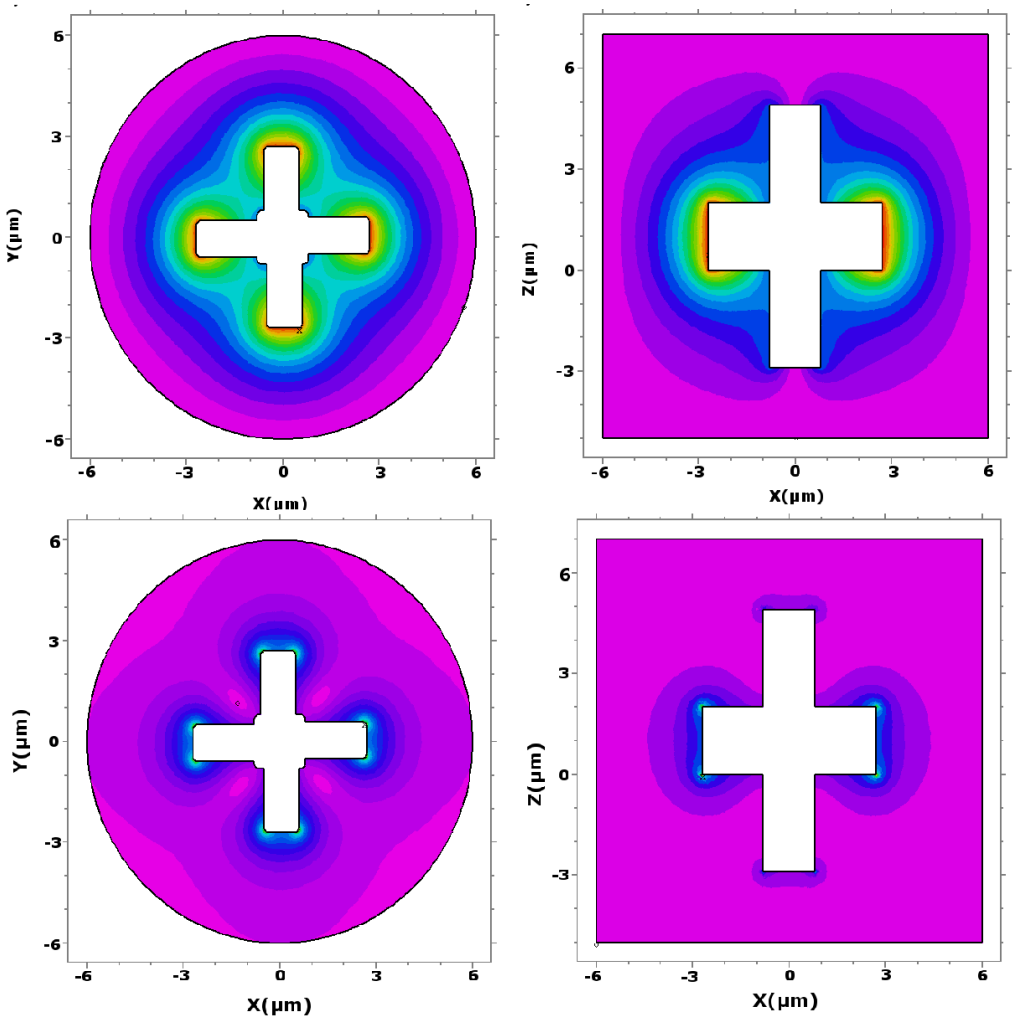

Figure 12. Typical graphical outputs of the FlexPDE program. Cross sections through x–y (a) and x–z (b) planes, respectively of the simulated flow field around the rotating particle. Similarly, the cross sections through the same planes for the shear stress field are depicted in (c) and (d), respectively.

While, in our calculation (and in our experiment), the ends of the cylinder enclosing the computational volume were sufficiently distant so as to not significantly influence the drag torque, the same method of calculation can still be used to find the torque even if the ends of the cylinder are close to the rotating structure. In this way, the influence of one or two nearby surfaces, above or below the structure, on the viscous drag can be determined. Thus, this method is of practical use even if a rotor is trapped next to a surface, or enclosed within a small chamber.

6.3. Evaluation of performance

The torques determined from all three methods—optical measurement (orbital torque efficiency of 0.2 and spin torque efficiencies of −0.02 (right circular), 0 (plane), and 0.03 (left circular), or an orbital torque of 4.8 ± 0.7 pN μm), computational electrodynamics (total torque efficiency

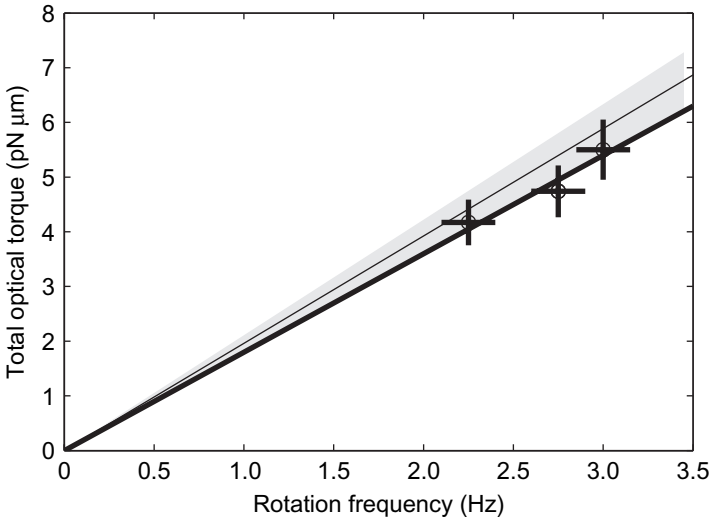

Figure 13. The total optical torque as a function of the rotation frequency (thick line). The simulated drag torque is also shown (thin line), with the error bound due to the experimental error in the frequency measurement (grey region).

of 0.2), and computational fluid dynamics (torque of 5.4 pN μm at 2.75 Hz, which was the rotation speed with the plane-polarized beam)—were in close agreement. The observed and predicted rotation rates are shown in figure 13.

One potential error in the electrodynamic calculation of the optical torque is the incident beam. The calculation as performed used a beam that approximated the actual beam as well as could be determined from measurement of the beam, but the results are sensitive to the details of the beam. This is compounded by the rapid variation of torque efficiency with axial position in the vicinity of the predicted axial equilibrium position.

Another source of error is heating due to absorption by the structure. Heating will result in changes in the viscosity of the surrounding fluid, reducing the drag torque, and will also result in convective flow in the fluid, which will displace the rotor upwards through viscous drag. The close agreement between the observed viscous drag and the computationally determined drag coefficient (which assumed a uniform temperature) suggests that any heating was minor. Only minor heating is expected, since preliminary measurements of the absorption coefficient of the photopolymerized resin show absorption close to that of water at 1070 nm. Nonetheless, there will be some heating present, and the effect can become important at high powers. The fact that the experimental data fit is close to the lower limit of the predicted values is likely to be due to heating of the structure and surrounding fluid by the trapping beam, which would decrease the viscosity, and hence the torque required for rotation at a given frequency.

The optical absorption force (absorption of linear momentum directly from the trapping beam) is much less likely to be important.

7. Further considerations for the design of optically driven microrotors

The orbital torque obtained here is 10 times higher than the spin component, which is a strong indication that these types of objects are suitable for OAM transfer. However, this is still less than the torque that can be achieved using strongly birefringent materials such as calcite or

vaterite (Bishop *et al* 2004), (but much higher than that obtained using shape birefringence or weakly birefringent materials).

From figure 10, we can see that torque efficiencies about three times higher can be obtained if the rotor is in the optimum axial position. If the rotor is mounted on a substrate, for example by an axle (Kelemen *et al* 2006), this can be achieved.

Secondly, as suggested in the discussion on design principles, microrotors that approximate blazed holograms will generate more torque.

Thirdly, there are fundamental physical limits to the available torque efficiency: a sufficiently large moment arm is still required, even if the azimuthal force acting on part of the rotor is produced by a beam of light. Thus, larger particles combined with larger focal spots can in principle allow higher torques (Courtial and Padgett 2000).

While the 'hologram picture' used here has been shown to be a useful method for the design of optically driven micromachines, the inherent limitations should be kept in mind. For the hologram view to be strictly correct, we would require thin structures and paraxial illumination. The first of these is not compatible with the requirement for a large phase difference between light that passes through the structure and light that does not, and the second is not compatible with the tightly focussed beams employed in optical tweezers. However, this hologram picture is a model that allows us to simply consider the effects of symmetry in the interaction between the beam and structure; the symmetry effects themselves do not depend on the hologram model being accurate. Therefore, we can expect this model to be successful qualitatively, but we should be prepared for the quantitative performance to differ from that expected. This reinforces the value of quantitative methods for testing the performance of prototype designs in practice, and methods for accurate quantitative modelling of the beam–structure interaction.

8. Conclusion

In conclusion, we have demonstrated that consideration of the effects of symmetry on the scattering of light provides a sound theoretical basis for the design of optically driven microrotors. In particular, it provides a simple set of qualitative guidelines for the development of initial designs that can then be experimentally or computationally evaluated. Rotors exploiting the OAM of light can make use of angular momentum fluxes of over $\hbar$ per photon in the driving beam, and can have higher efficiencies as a result; in our example case in this paper, the orbital component of the torque was ten times higher than the spin torque.

The total optical torque exerted on micrometer sized objects rotating in an optical trap can be measured accurately by optical means, by polarimetric measurement of the spin component of the optical torque. Even when the orbital component of the torque is much greater than the spin torque, as it was in our test of the method here, the results are accurate.

We have also demonstrated an efficient method for calculating the viscous drag torque acting on such a microrotor, computationally solving the 3D Laplace equation. This can be used for finding the optical torque acting on a microrotor from the rotation rate, as we did here, or for the prediction of performance, including near a surface.

The two-photon photopolymerization technique has proved to be a powerful tool for fabricating microstructures with potentially any arbitrary shape, which can be useful in studies dealing with transfer of linear and/or angular optical momentum. While it might not be the method of choice for the large-scale manufacture of devices, it is perfect for the fabrication of prototypes and test devices.

It is the synergistic combination of these methods that allows the rapid design, testing, and evaluation of optically driven rotating microdevices. Coupled with rigorous modelling of the electromagnetic forces and torques and, ideally, resulting non-electromagnetic effects such as heating and convective flow, the engineering and design of such micromachines can be carried out in a systematic and guided manner.

References

Allen L, Beijersbergen M W, Spreeuw R J C and Woerdman J P 1992 *Phys. Rev.* A **45** 8185–9

Asavei T, Nieminen T A, Heckenberg N R and Rubinsztein-Dunlop H 2009 *J. Opt.* A **11** 034001

Ashkin A, Dziedzic J M, Bjorkholm J E and Chu S 1986 *Opt. Lett.* **11** 288–90

Bingelyte V, Leach J, Courtial J and Padgett M 2003 *Appl. Phys. Lett.* **82** 829–31

Bishop A I, Nieminen T A, Heckenberg N R and Rubinsztein-Dunlop H 2003 *Phys. Rev.* A **68** 033802

Bishop A I, Nieminen T A, Heckenberg N R and Rubinsztein-Dunlop H 2004 *Phys. Rev. Lett.* **92** 198104

Cheng Z, Chaikin P M and Mason T G 2002 *Phys. Rev. Lett.* **89** 108303

Courtial J and Padgett M J 2000 *Opt. Commun.* **173** 269–74

Denk W, Strickler J H and Webb W W 1990 *Science* **248** 73–6

Deufel C, Forth S, Simmons C R, Dejgosha S and Wang M D 2007 *Nat. Method.* **4** 223–5

FlexPDE 5.0 User Guide 2005 (Antioch, CA: PDE Solutions)

Friese M E J, Nieminen T A, Heckenberg N R and Rubinsztein-Dunlop H 1998 *Nature* **394** 348–50

Friese M E J, Nieminen T A, Heckenberg N R and Rubinsztein-Dunlop H 1998 *Nature* **395** 621 (erratum)

Galajda P and Ormos P 2001 *Appl. Phys. Lett.* **78** 249–51

Galajda P and Ormos P 2002 *Appl. Phys. Lett.* **80** 4653–5

Gauthier R C 2001 *Appl. Opt.* **40** 1961–73

He H, Friese M E J, Heckenberg N R and Rubinsztein-Dunlop H 1995a *Phys. Rev. Lett.* **75** 826–9

He H, Heckenberg N R and Rubinsztein-Dunlop H 1995b *J. Mod. Opt.* **42** 1, 217–23

Heckenberg N R, McDuff R, Smith C P, Rubinsztein-Dunlop H and Wegener M J 1992a *Opt. Quantum Electron.* **24** S951–62

Heckenberg N R, McDuff R, Smith C P and White A G 1992b *Opt. Lett.* **17** 221–3

Higurashi E, Ukita H, Tanaka H and Ohguchi O 1994 *Appl. Phys. Lett.* **64** 2209–10

Kelemen L, Valkai S and Ormos P 2006 *Appl. Opt.* **45** 2777–80

Knöner G, Parkin S, Nieminen T A, Loke V L Y, Heckenberg N R and Rubinsztein-Dunlop H 2007 *Opt. Express* **15** 5521–30

Loke V L Y, Nieminen T A, Heckenberg N R and Rubinsztein-Dunlop H 2009 *J. Quant. Spectrosc. Radiat. Transfer* **110** 1460–71

Maruo S and Fourkas J T 2008 *Laser Photon. Rev.* **2** 100–11

Maruo S, Ikuta K and Korogi H 2003 *Appl. Phys. Lett.* **82** 133–5

Maruo S and Inoue H 2006 *Appl. Phys. Lett.* **89** 144101

Maruo S, Nakamura O and Kawata S 1997 *Opt. Lett.* **22** 132–4

Mishchenko M I, Hovenier J W and Travis L D (ed) 2000 *Light Scattering by Nonspherical Particles: Theory, Measurements, and Applications* (New York: Academic)

Moffitt J R, Chemla Y R, Smith S B and Bustamante C 2008 *Annu. Rev. Biochem.* **77** 205–28

Nieminen T A, Asavei T, Loke V L Y, Heckenberg N R and Rubinsztein-Dunlop H 2009 *J. Quant. Spectrosc. Radiat. Transfer* **110** 1472–82

Nieminen T A, Heckenberg N R and Rubinsztein-Dunlop H 2001 *J. Mod. Opt.* **48** 405–13

Nieminen T A, Loke V L Y, Stilgoe A B, Knöner G, Brańczyk A M, Heckenberg N R and Rubinsztein-Dunlop H 2007 *J. Opt.* A **9** S196–203

Nieminen T A, Parkin S J, Heckenberg N R and Rubinsztein-Dunlop H 2004 *Proc. SPIE* **5514** 254–63

Nieminen T A, Rubinsztein-Dunlop H and Heckenberg N R 2003 *J. Quant. Spectrosc. Radiat. Transfer* **79–80** 1005–17
Nieminen T A, Stilgoe A B, Heckenberg N R and Rubinsztein-Dunlop H 2008 *J. Opt.* A **10** 115005
Park S H, Yang D Y and Lee K S 2009 *Laser Photon. Rev.* **3** 1–11
Parkin S J, Nieminen T A, Heckenberg N R and Rubinsztein-Dunlop H 2004 *Phys. Rev.* A **70** 023816
Parkin S, Knöner G, Nieminen T A, Heckenberg N R and Rubinsztein-Dunlop H 2006 *Opt. Exp.* **14** 6963–70
Parkin S J, Knöner G, Nieminen T A, Heckenberg N R and Rubinsztein-Dunlop H 2007 *Phys. Rev.* E **76** 041507
Paterson L, MacDonald M P, Arlt J, Sibbett W, Bryant P E and Dholakia K 2001 *Science* **292** 912–4
Sato S, Ishigure M and Inaba H 1991 *Electron. Lett.* **27** 1831–2
Strickler J H and Webb W W 1991 *Opt. Lett.* **16** 1780–2
Ukita H and Kanehira M 2002 *IEEE J. Sel. Top. Quantum Electron.* **8** 111–7
Ukita H and Nagatomi K 2003 *Appl. Opt.* **42** 2708–15
Waterman P C 1971 *Phys. Rev.* D **3** 825–39